

Chemistry–A European Journal

Supporting Information

pH Tuning of Water-Soluble Arylazopyrazole Photoswitches

Simon Ludwanowski,^[a, b, c] Meral Ari,^[c] Karsten Parison,^[a] Somar Kalthoum,^[c] Paula Straub,^[a]
Nils Pompe,^[e] Stefan Weber,^[e] Michael Walter,^{*[c, d]} and Andreas Walther^{*,[a, b, c, d]}

Materials

All chemicals were bought and used without further purification: Aniline (VWR Internationals, >99.5 %), sodium nitrite (Abcr, >97.0 %), hydrazine monohydrate (Abcr, >98.0 %), methyl bromoacetate (Sigma-Aldrich, 97.0 %), lithium hydroxide (Carl Roth, >95.0 %), *Boc*-TOTA (1-(*t*-butyloxycarbonylamino)-4,7,10-trioxa-13-tridecanamine, Iris Biotech), DMAP (4-dimethylamino-pyridine, Sigma-Aldrich, >99.0 %), 1-ethyl-3-(3-dimethylaminopropyl)-carbodiimide hydrochloride (EDC·HCl, Abcr, 98.0 %), trifluoroacetic acid (Abcr, 99.0 %), acryloyl chloride (Abcr, 97.0 %), OEGMA (oligo ethylene glycol) methyl ether methacrylate, $M_w = 500 \text{ g}\cdot\text{mol}^{-1}$, Sigma-Aldrich), sodium 4-vinylbenzenesulfonate (4VBS, Sigma-Aldrich, $\geq 90.0 \%$).

Instrumentation

NMR spectroscopy

NMR measurements were conducted on a 300 MHz (7.0 T) Bruker ARX 300 spectrometer. NMR experiments with *in-situ* irradiation were performed on a 600 MHz (14.1 T) Bruker Avance III HD spectrometer. Samples were irradiated with fiber coupled LEDs from Ocean Optics. Coupling constants J and chemical shifts δ are displayed in Hz and in ppm, respectively. The signals of deuterated solvents were used as internal standards.

Mass spectrometry

Mass spectrometric analyses were conducted using an LCQ Advantage from Thermo Scientific *via* electrospray ionization (ESI) or atmospheric pressure chemical ionization (APCI).

UV/Vis spectroscopy

Absorption measurements were carried out on an QE Pro from Ocean Optics equipped with the light source DH-2000-BAL and a temperature-controlled cuvette holder. Time-resolved measurements were acquired using self-written MatLab scripts.

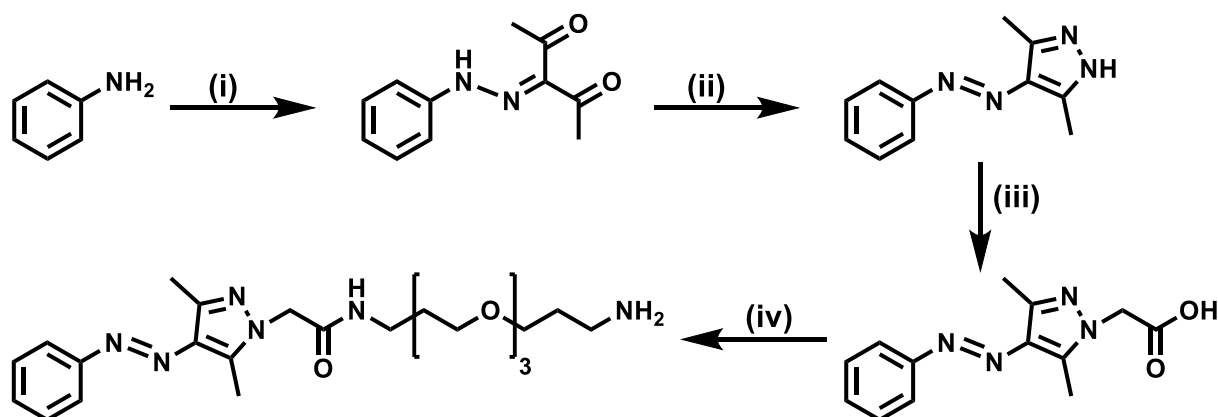
LED set-up

Samples were irradiated with fiber-coupled LEDs from Mightex (365 nm: $374 \pm 4.7 \text{ nm}$, 80 mW and 530 nm: $545 \pm 16 \text{ nm}$, 100 mW) and Ocean Optics (365 nm: $371 \pm 4.6 \text{ nm}$, 1 mW and 530 nm: $538 \pm 18 \text{ nm}$, 0.75 mW).

pH measurements

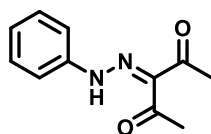
pH measurements were carried out on a 907 Titrand from Metrohm.

Synthesis



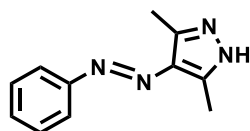
Scheme S1. Synthesis of water-soluble PEG-AAP. Reaction conditions: (i) NaNO_2 , HCl , AcOH , 2,4-pentadione, NaOAc , 57 %; (ii) hydrazine hydrate, 100 %; (iii) (1) methyl bromoacetate, K_2CO_3 , (2) LiOH , 89 %; (iv) (1) *Boc*-TOTA, EDC, DMAP; (2) TFA, K_2CO_3 , 49 %.

Synthesis of 3-(2-phenylhydrazono)pentane-2,4-dione



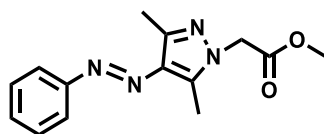
Aniline (5.50 g, 59.1 mmol) was dissolved in AcOH (90 mL) and conc. HCl (13.6 mL) and cooled to 0°C . NaNO_2 (4.92 g, 71.2 mmol, 1.2 eq.) dissolved in a minimum amount of water was added dropwise and the solution was stirred at 0°C for 45 min. The resulting diazonium salt was transferred to a solution of pentane-2,4-dione (7.73 g, 76.8 mmol, 1.3 eq.) and NaOAc (17.5 g, 213 mmol, 3.0 eq.) in EtOH (30 mL) and water (17 mL) at 0°C . The mixture was warmed to RT and stirred for 1 h. Afterwards, the mixture was mixed with ice to increase precipitation and the yellow solid was isolated *via* vacuum filtration. After washing with water, water / EtOH (1:1 v/v) and hexane the precipitate was dried under vacuum to yield the desired compound as a yellow solid. Yield: 6.85 g (33.6 mmol, 56.8 %). $^1\text{H-NMR}$ (CDCl_3 , 300 MHz, 25°C): δ = 7.42 (m, 4H), 7.21 (m, 1H), 2.61 (s, 3H), 2.50 (s, 3H) ppm. ESI-MS(+) calculated for $\text{C}_{11}\text{H}_{13}\text{N}_2\text{O}_2^+$ [$\text{M} + \text{H}$] $^+$: 205.0972 $\text{g}\cdot\text{mol}^{-1}$. ESI-MS(+) found: 205.0974 $\text{g}\cdot\text{mol}^{-1}$.

Synthesis of AAP (arylazo-bis(o-methylated)-pyrazole)



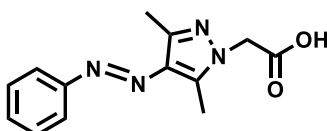
3-(2-phenylhydrazono)pentane-2,4-dione (6.85 g, 33.6 mmol) was dissolved in EtOH (100 mL) and hydrazine monohydrate (1.80 mL, 1.85 g, 36.9 mmol, 1.1 eq.) was added dropwise. Subsequently, the reaction mixture was refluxed for 3 h. The solvent was removed *in vacuo* and the product was obtained as a yellow solid. Yield: 6.70 g (33.5 mmol, 99.8 %). $^1\text{H-NMR}$ (CDCl_3 , 300 MHz, 25°C): δ = 8.87 (s, 1H), 7.80 (m, 2H), 7.48 (m, 2H), 7.39 (m, 1H), 2.61 (s, 6H) ppm.

Synthesis of AAP-AcOMe



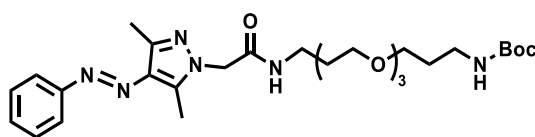
AAP (6.70 g, 33.5 mmol) and K_2CO_3 (13.9 g, 101 mmol, 3.0 eq.) were dispersed in anhydrous ACN under nitrogen. Methyl bromoacetate (4.20 mL, 6.80 g, 44.5 mmol, 1.3 eq.) was added dropwise and the reaction mixture was refluxed for 18 h. The solvent was removed under reduced pressure and the resulting solid was re-dissolved in EtOAc / H_2O (1:1 v/v). The aqueous phase was extracted with EtOAc (4 x 20 mL) and dried over $MgSO_4$. EtOAc was removed under reduced pressure to yield a brown solid which was purified using column chromatography (SiO_2 , DCM / MeOH, 98:2). Yield: 8.84 g (32.5 mmol, 97.0 %). 1H -NMR ($CDCl_3$, 300 MHz, 25 °C): δ = 7.73 (m, 2H), 7.40 (tt, J = 6.7, 1.0 Hz, 2H), 7.32 (m, 1H), 4.80 (s, 2H), 3.73 (s, 3H), 2.50 (s, 3H), 2.45 (s, 3H) ppm. ESI-MS(+) calculated for $C_{14}H_{17}N_4O_2^+$ [$M + H$] $^+$: 273.1346 $g \cdot mol^{-1}$. ESI-MS(+) found: 273.1345 $g \cdot mol^{-1}$.

Ester hydrolysis to prepare AAP-AcOH



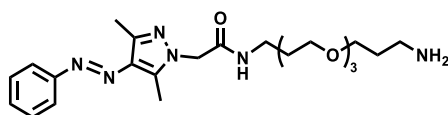
AAP-AcOH (5.00 g, 18.4 mmol) was dissolved in THF / water (150 mL, 4:1, v/v) and LiOH (660 mg, 27.5 mmol, 1.5 eq.) was added. Afterwards, the solution was stirred at RT for 14 h. THF was removed under reduced pressure and the aqueous phase was extracted with EtOAc (1 x 20 mL). The organic phase was discarded, and the aqueous phase was acidified with conc. HCl to pH = 1 – 2. Subsequently, the aqueous phase was extracted with EtOAc (3 x 50 mL) and the combined organic layers were dried over $MgSO_4$. The solvent was removed *in vacuo* yielding the product as a yellow solid. Yield: 4.37 g (16.9 mmol, 92.1 %). 1H -NMR ($DMSO-d_6$, 300 MHz, 25 °C): δ = 13.25 (s, 1H), 7.74 (m, 2H), 7.54 (m, 2H), 7.44 (m, 1H), 4.96 (s, 2H), 2.52 (s, 3H), 2.39 (s, 3H) ppm. APCI-MS(+) calculated for $C_{13}H_{15}N_4O_2^+$ [$M + H$] $^+$: 259.1190 $g \cdot mol^{-1}$. APCI-MS(+) found: 259.1187 $g \cdot mol^{-1}$.

Synthesis of AAP-PEG-NH-Boc



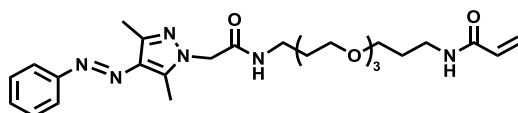
Boc-TOTA (4.49 g, 14.0 mmol, 1.3 eq.) was dissolved in dioxane and DCM (60 mL, 5:1) and mixed with AAP-AcOH (2.83 g, 11.0 mmol). EDC-HCl (6.23 g, 32.5 mmol, 3.0 eq.) and DMAP (3.98 g, 32.6 mmol, 3.0 eq.) were added subsequently. The reaction was stirred at RT for 14 h. Afterwards the solution was concentrated *in vacuo* and the residue was dissolved in EtOAc. The solution was washed with saturated $NaHCO_3$ solution and the solvent was removed under reduced pressure. The resulting oil was purified using column chromatography (SiO_2 , DCM / MeOH, 8:2) and AAP-PEG-NH-Boc was obtained as an orange oil. Yield: 4.14 g (7.38 mmol, 67.3 %). 1H -NMR ($CDCl_3$, 300 MHz, 25 °C): δ = 7.77 (m, 2H), 7.46 (m, 2H), 7.37 (m, 1H), 6.54 (s, 1H), 4.97 (s, 1H), 4.71 (s, 2H), 3.54 (m, 11H), 3.36 (p, J = 5.7, 5.3 Hz, 2H), 3.18 (q, J = 6.3 Hz, 2H), 2.58 (s, 3H), 2.51 (s, 3H), 1.73 (m, 4H), 1.41 (s, 9H) ppm.

Boc-deprotection to prepare AAP-PEG-NH₂ (abbreviated PEG-AAP)



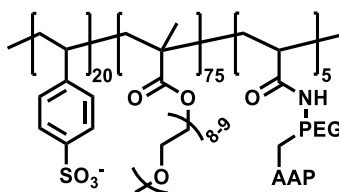
AAP-PEG-NH-*Boc* (4.14 g, 7.38 mmol) was dissolved in DCM (30 mL) and the solution was cooled to 0 °C. Trifluoroacetic acid (15 mL) was added dropwise and the solution was stirred at RT for 3 h. The solvent was removed under reduced pressure and the resulting oil was dissolved in water and washed with EtOAc (3 x 5 mL). Afterwards, the water was removed *via* freeze drying and the desired product was obtained as the TFA salt. Subsequently, it was dissolved in aq. K₂CO₃ (1 wt%), extracted with DCM and the combined organic phases were dried over MgSO₄. Removing the solvent *in vacuo* yielded the desired product as a yellow-orange solid. Yield: 2.52 g (5.46 mmol, 74.1 %). ¹H-NMR (D₂O, 300 MHz, 25 °C): δ = 7.48 (m, 2H), 7.17 (m, 3H), 4.62 (s, 2H), 3.58 (m, 14H), 3.26 (t, *J* = 6.8 Hz, 2H), 3.08 (dt, *J* = 21.5, 7.3 Hz, 2H), 2.27 (s, 3H), 2.23 (s, 3H), 1.82 (m, 4H) ppm. ¹³C-NMR (D₂O, 75 MHz, 25 °C): δ = 167.81, 152.65, 142.63, 140.93, 134.39, 129.47, 128.65, 121.55, 118.26, 114.39, 69.38, 69.28, 69.21, 68.20, 50.98, 37.60, 36.58, 28.26, 26.41, 13.01, 9.04 ppm. ESI-MS(+) calculated for C₂₃H₃₇N₆O₄⁺ [M + H]⁺: 461.2871 g·mol⁻¹. ESI-MS(+) found: 461.2869 g·mol⁻¹.

Preparation of AAP-PEG-AAm



AAP-PEG-NH₂ (46.0 mg, 0.100 mmol) was dissolved in DCM (15 mL), nitrogen-purged (10 min) and cooled to 0 °C with an ice bath. The yellow solution was mixed dropwise with acryloyl chloride (11.2 mg, 0.124 mmol, 1.24 eq.) dissolved in DCM (5 mL) at 0 °C while keeping a nitrogen atmosphere. The reaction mixture was warmed to RT and stirred overnight in the dark. Afterwards, it was quenched with water (5 mL) and stirred for further 5 min. The reaction mixture was transferred with DCM (10 mL) and mixed with aq. Na₂CO₃ (5 mL, 10 wt%). The aqueous phase was extracted with DCM (2 x 10 mL). The combined organic phases were dried over MgSO₄ and subsequently, the solvent was removed *in vacuo* to yield the desired product. Yield: 46.3 mg (90.0 μ mol, 90.1 %). ¹H-NMR (CDCl₃, 300 MHz, 25 °C): δ = 7.78 (m, 2H), 7.46 (m, 2H), 7.35 (m, 1H), 6.23 (dd, *J* = 17.0, 1.8 Hz, 1H), 6.06 (dd, *J* = 17.0, 10.1 Hz, 1H), 5.56 (dd, *J* = 10.1, 1.8 Hz, 1H), 4.71 (d, *J* = 2.0 Hz, 2H), 3.53 (m, 12H), 3.37 (m, 4H), 2.59 (d, *J* = 6.1 Hz, 3H), 2.50 (d, *J* = 3.0 Hz, 3H), 1.75 (dp, *J* = 12.3, 6.0 Hz, 4H) ppm.

Preparation of AAP-polymer (AAP-PEG-AAm-co-PEGMA-co-4VBS)



AAP-PEG-AAm (23.5 mg, 0.0457 mmol, 5 mol-%) was dissolved in OEGMA (351.1 mg, *M_w* = 500 g·mol⁻¹, 0.702 mmol, 75 mol-%) and mixed with 4VBS (41.9 mg, 0.183 mmol, 20 mol-%). Subsequently, the monomers were mixed in water (35 mL) and ethanol (5 mL), nitrogen-purged (10 min), and mixed with aqueous potassium

persulfate solution (2 mL, 4 mg·mL⁻¹). The yellow dispersion was heated to 70 °C and stirred for 5 h under an atmosphere of nitrogen, resulting in a yellow solution of AAP-polymer.

Film casting CNC & AAP-polymer

The previously prepared AAP-polymer (6.0 mL, 1.0 wt%) was dropwise mixed with an aqueous dispersion of cellulose nanocrystals, prepared as reported previously (CNC, 6.0 mL, 0.2 wt%).^[1] The pH was adjusted to 4.0 and 7.4 using aqueous NaOH solution (0.1 M). The films were cast at 50 °C in a vacuum oven (700 mbar) for 1 day.

Determination of the PSD

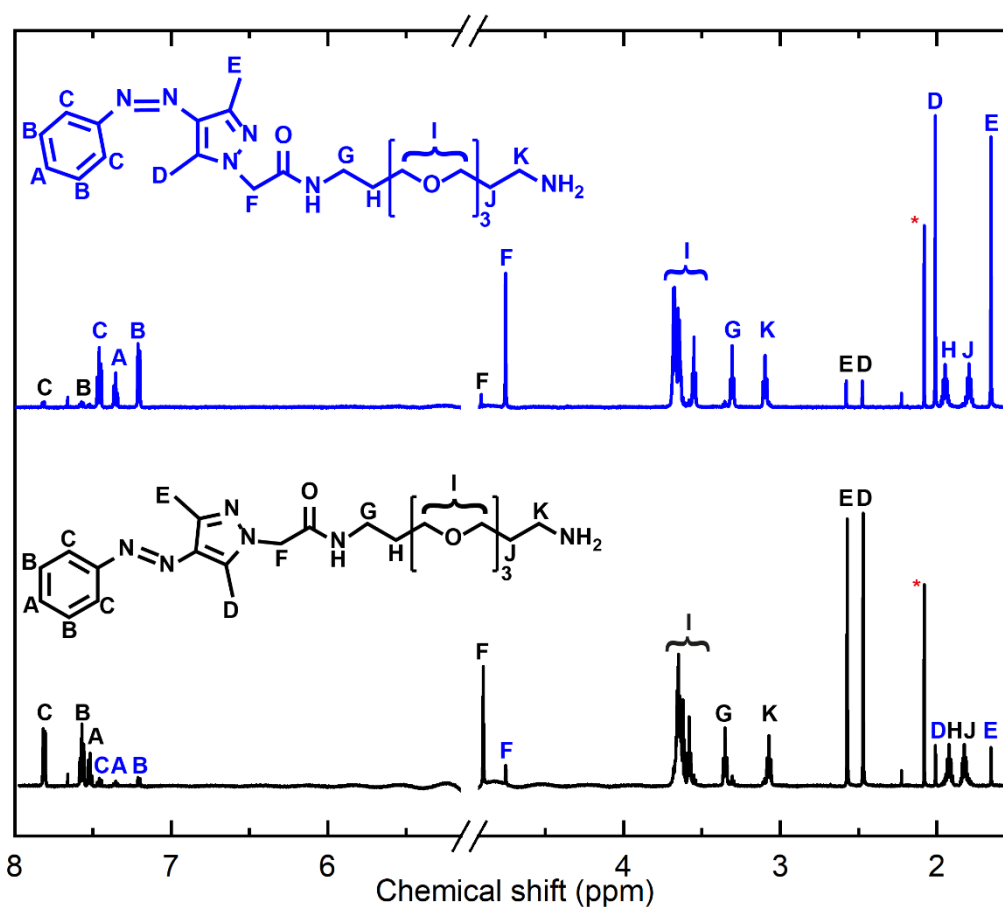


Figure S1. Determination of the PSD of *E*- and *Z*-PEG-AAP in D₂O using ¹H-NMR. The integration of the aromatic peaks (A, B, C) as well as the pyrazole methyl groups (D, E) of both isomers results a photostationary state of PSS^{365 nm} = 91 % (blue) and PSS^{530 nm} = 95 % (black). The solvent residual signal was cut from the spectra and acetonitrile (highlighted by a red star) was used as internal standard ($\delta = 2.06$ ppm).

Spectra of *E*- and *Z*-PEG-AAP as a function of pH

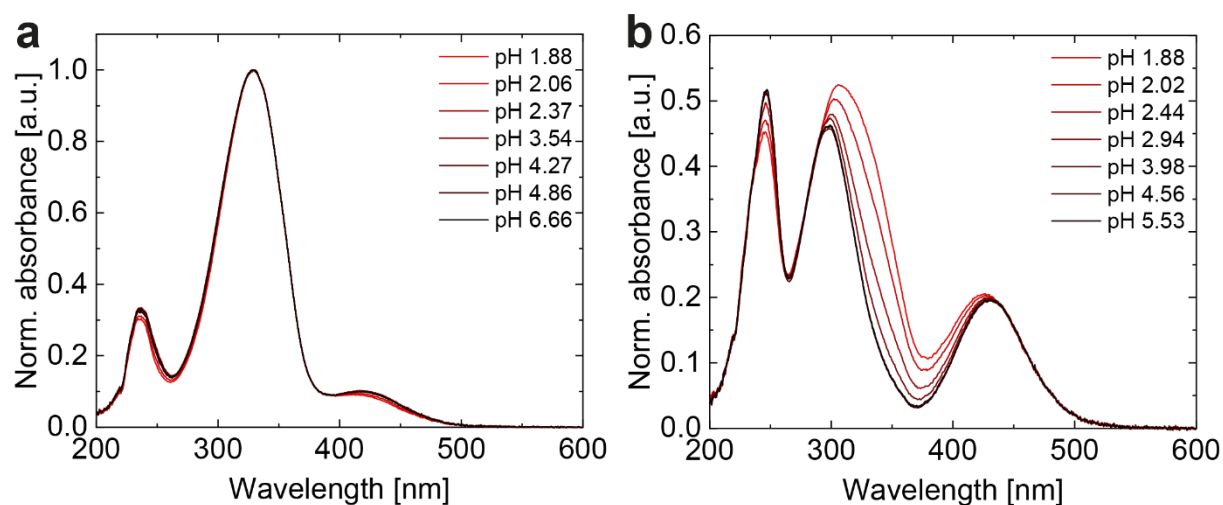


Figure S2: UV-Vis spectra of *E*- and *Z*-PEG-AAP as function of pH. (a) The UV-Vis spectra of *E*-AAP hardly change down to pH 2. (b) After irradiation with 365 nm, the UV-Vis spectra of the *Z*-APP show that the separation of the π - π^* and the n - π^* transitions decreases with decreasing pH which leads to a lower PSD.

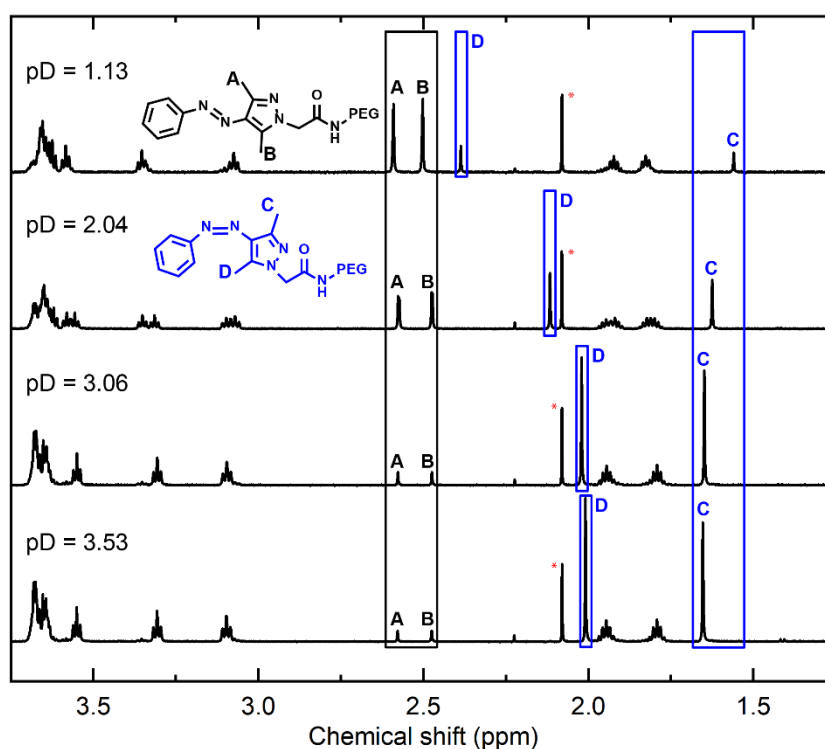


Figure S3: PSD of *Z*-PEG-AAP as function of pD determined by ¹H-NMR. The spectra were recorded in D₂O on a Bruker 600 MHz NMR spectrometer at 5 °C after irradiation with an Ocean Optics LED (365 nm, 1 mW, 10 min). The chemical shift of acetonitrile highlighted by a red star was set as reference ($\delta = 2.06$ ppm) because the solvent residual signal of D₂O strongly varies with varying pD. The signals of the methyl groups of *Z*-AAP distinctly shift as function of pD as opposed to the signals of *E*-AAP, which indicates that *Z*-AAP is more basic than *E*-AAP. The PSD was determined by the integration of the signals of methyl groups of *Z*- (blue boxes) and *E*-AAP (black box).

Table S1: PSD as function of pD. The PSD decreases in the strongly acidic regime (pD < 3.0).

pD ()	$PSD_{365\text{nm}}(\text{Z-AAP})$ (%)	$PSD_{365\text{nm}}(\text{E-AAP})$ (%)
1.13	20.4	79.6
2.04	54.3	45.7
2.86	88.5	11.5
3.53	90.7	9.3

Linearized Eyring plots

The pH of a 100 μM AAP solution was adjusted using suitable buffer (citric acid, phosphate, 10 mM) with NaOH (0.1 M) and HCl (0.1 M). Subsequently, the cuvette (3.5 mL) was filled with the AAP solution (3.0 mL) and sealed with a PTFE stopper to prevent evaporation. Under continuous stirring, the sample was irradiated with a Mightex UV LED ($\lambda_{\text{center}} = 373.5 \text{ nm}$, 80 mW) fiber-coupled to a liquid light guide for 10 minutes. Subsequently, time-resolved UV-Vis spectra were recorded at different temperatures while keeping the samples in the dark. After baseline correction by a self-written MatLab script, the absorbance $A_{335 \text{ nm}}$ at 335 nm was plotted against the time t . The reaction rate constant k was directly calculated by a monoexponential decay fit function (1), assuming first order kinetics. The offset $A_{0,335 \text{ nm}}$ of the fit function was set constant to the absorbance of the *E*-isomer at 335 nm, whereas $\Delta A_{0,335 \text{ nm}}$ represents the difference in absorbance between the *E*- and the *Z*-isomer at the respective PSS. In case of first order kinetics, equation (2) relates the reaction rate constant k and the thermal half-life $\tau_{1/2}$ which is defined as the time needed to switch 50 % of *Z*-AAP back to the *E*-isomer.

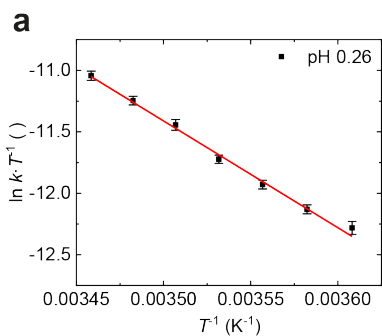
$$A_{335 \text{ nm}}(t) = \Delta A_{0,335 \text{ nm}} \cdot \exp(-k \cdot t) + A_{0,335 \text{ nm}}(\text{E-AAP}) \quad (1)$$

$$\tau_{1/2} = \frac{\ln 2}{k} \quad (2)$$

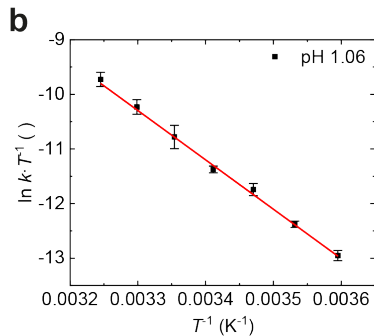
The relaxation rate constants k , which were calculated by the monoexponential fit (1), were determined at seven different temperatures (5 – 85 °C), depending on how fast the relaxation proceeds. The logarithmic relaxation rate constants divided by T ($\ln k \cdot T^{-1}$) were subsequently plotted against the inverse thermodynamic temperature T^{-1} and fitted by the linearized Eyring equation (3). With the aid of the resulting slope m and the y -intercept c , the thermal half-life $\tau_{1/2}(25 \text{ °C})$ was obtained according to equation (2) and (4).

$$\ln \frac{k}{T} = - \frac{\Delta H^\ddagger}{R \cdot T} + \frac{\Delta S^\ddagger}{R} + \ln \frac{k_B}{h} \quad (3)$$

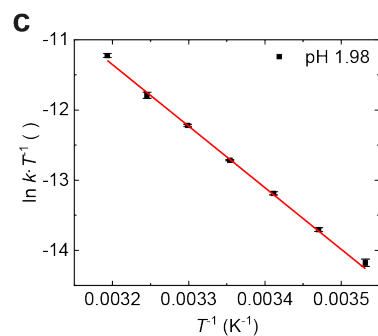
$$k(25 \text{ °C}) = T \cdot \exp\left(\frac{1}{T} \cdot m + c\right) \quad (4)$$



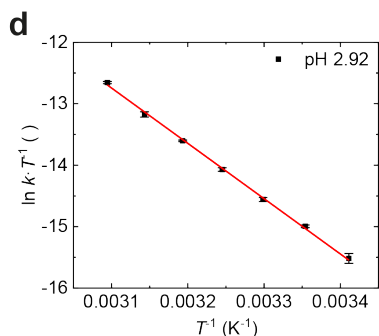
m (K)	c ()
- 8689.06193	19.00033
± 275.76997	± 0.97291



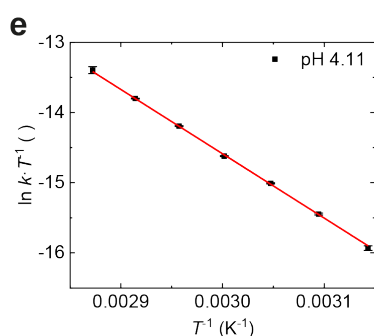
m (K)	c ()
- 9037.69478	19.52875
± 246.68624	± 0.85448



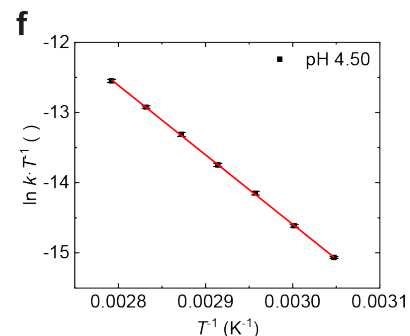
m (K)	c ()
- 8766.47884	16.69793
± 174.41022	± 0.58427



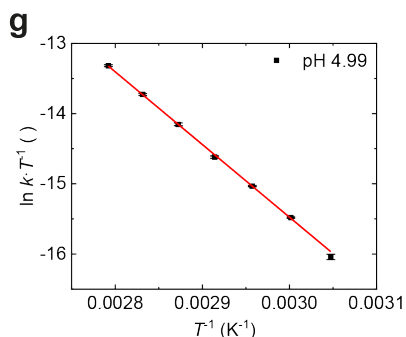
m (K)	c ()
- 9003.77000	15.16716
± 149.36712	± 0.47982



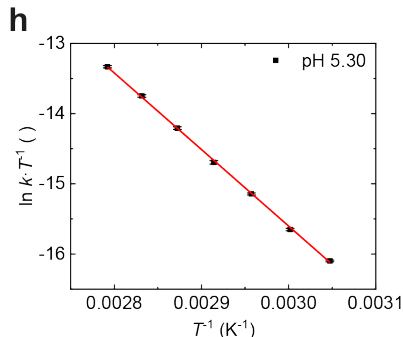
m (K)	c ()
- 9160.11209	12.89247
± 75.7065	± 0.22459



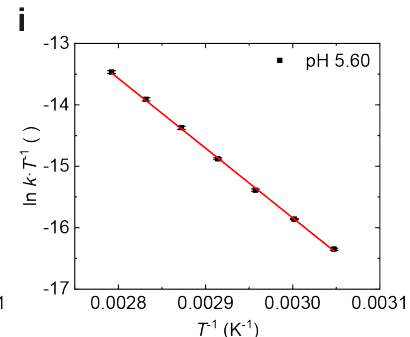
m (K)	c ()
- 9892.55317	15.08545
± 46.09813	± 0.13555



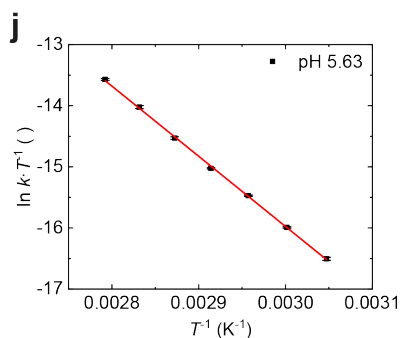
m (K)	c ()
- 10355.57611	15.59101
± 91.87683	± 0.26884



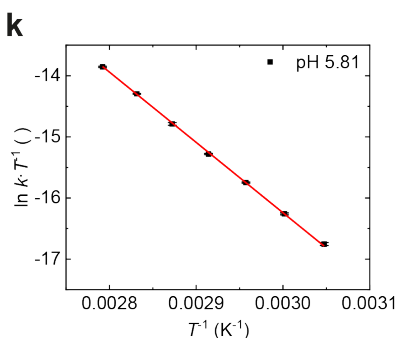
m (K)	c ()
- 10901.28575	17.10213
± 89.77483	± 0.26334



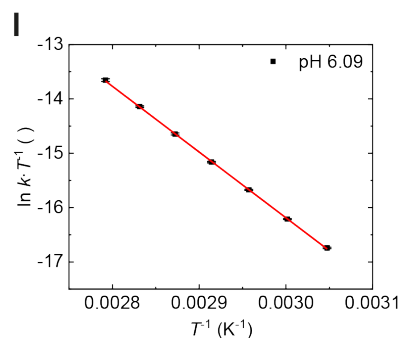
m (K)	c ()
- 11348.36198	18.20489
± 106.64759	± 0.31515



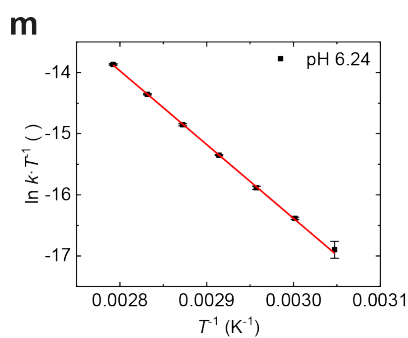
m (K)	c ()
-11478.59352	18.46039
± 114.48647	± 0.33543



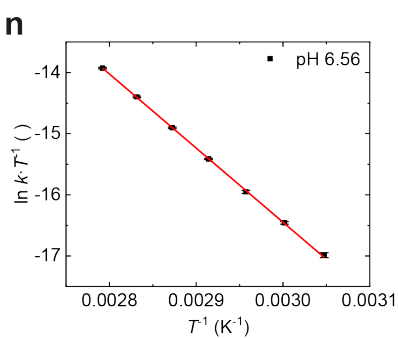
m (K)	c ()
-11507.63943	18.28134
± 82.70888	± 0.23839



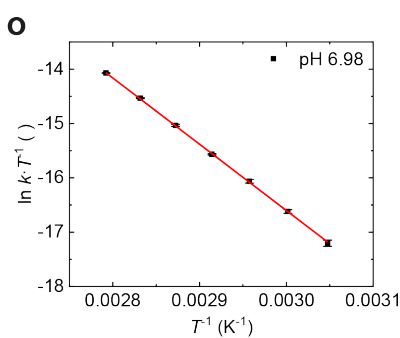
m (K)	c ()
-12102.70892	20.12030
± 61.36907	± 0.18071



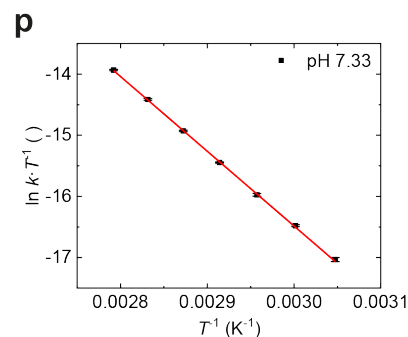
m (K)	c ()
-12063.65103	19.80645
± 62.03138	± 0.17842



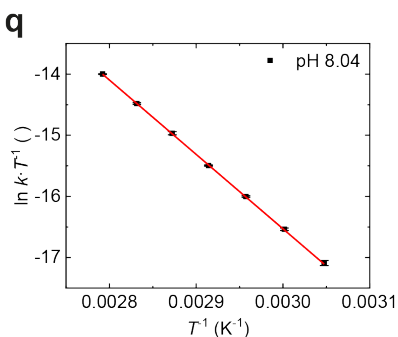
m (K)	c ()
-12123.50864	19.92247
± 59.22481	± 0.17040



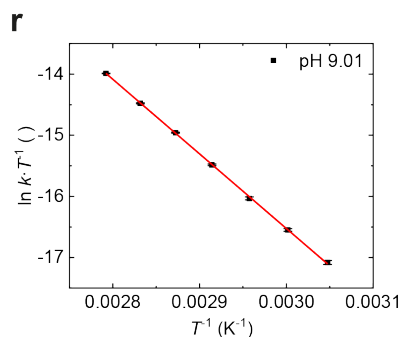
m (K)	c ()
-12194.66101	19.98249
± 76.85456	± 0.21719



m (K)	c ()
-12230.19160	20.20573
± 86.69711	± 0.25047



m (K)	c ()
-12168.80139	19.97597
± 41.16345	± 0.11725



m (K)	c ()
-12207.00950	20.09491
± 59.14373	± 0.16815

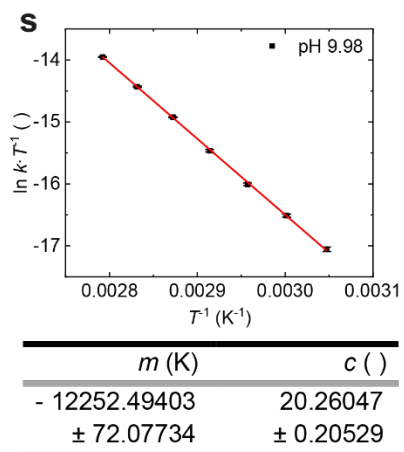


Figure S4. Linearized Eyring plots as a function of pH.

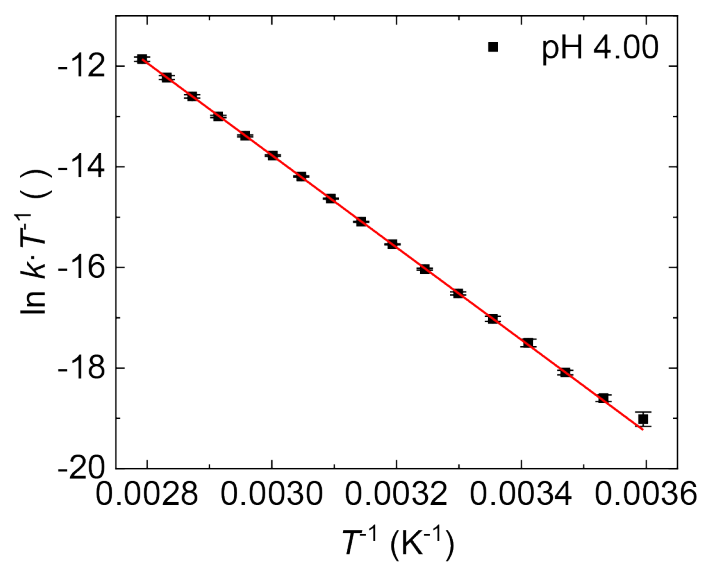


Figure S5: Linearized Eyring plot from 5 °C to 85 °C in citric acid buffer (10 mM, pH = 4.00).

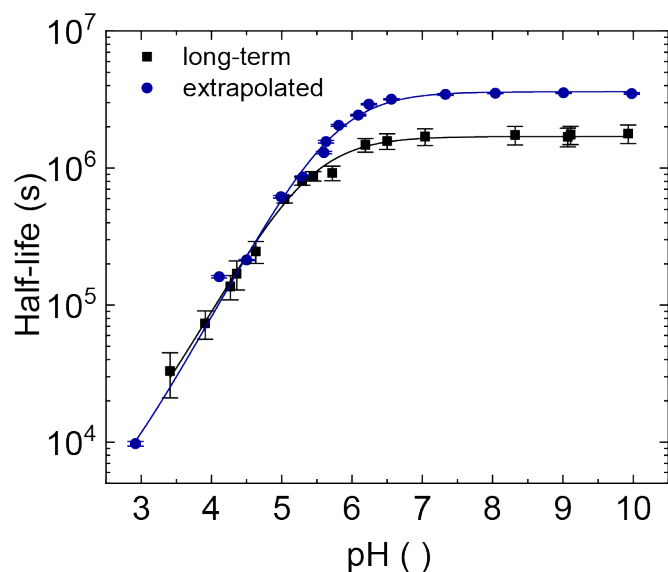
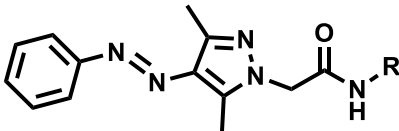
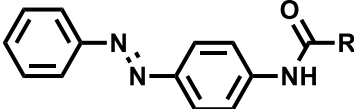
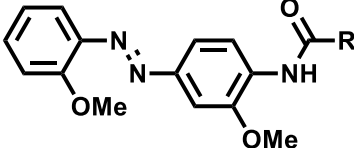
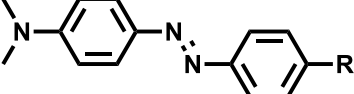


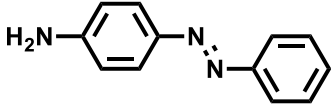
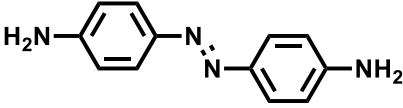
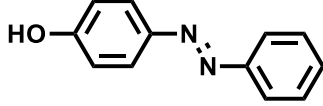
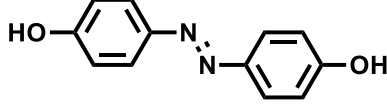
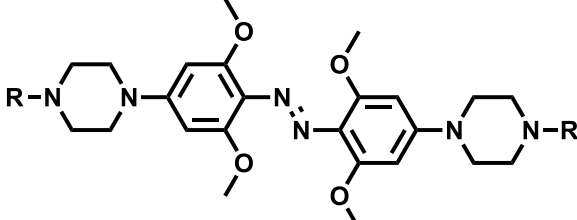
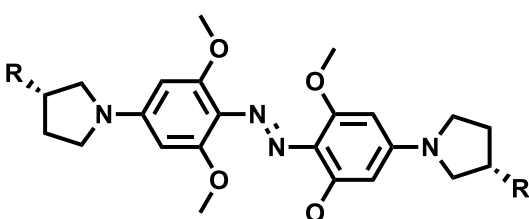
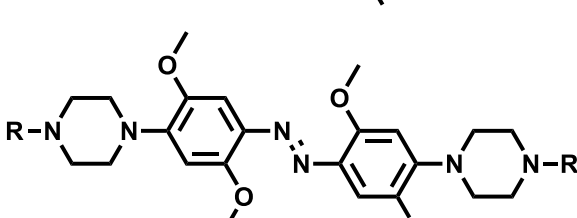
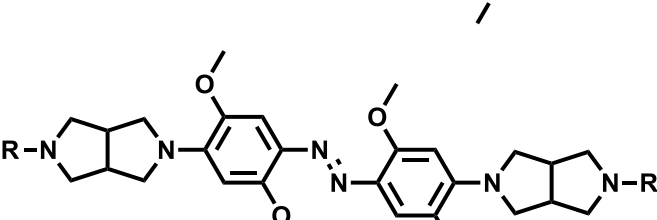
Figure S6. Comparison of long-term measured and extrapolated half-lives at 23 °C. The extrapolated half-lives are generally higher than the measured ones. Nevertheless, they illustrate the exact same trend and are in the same order of magnitude.

Comparison of pH-dependent tunability of half-lives of AAP and azobenzenes

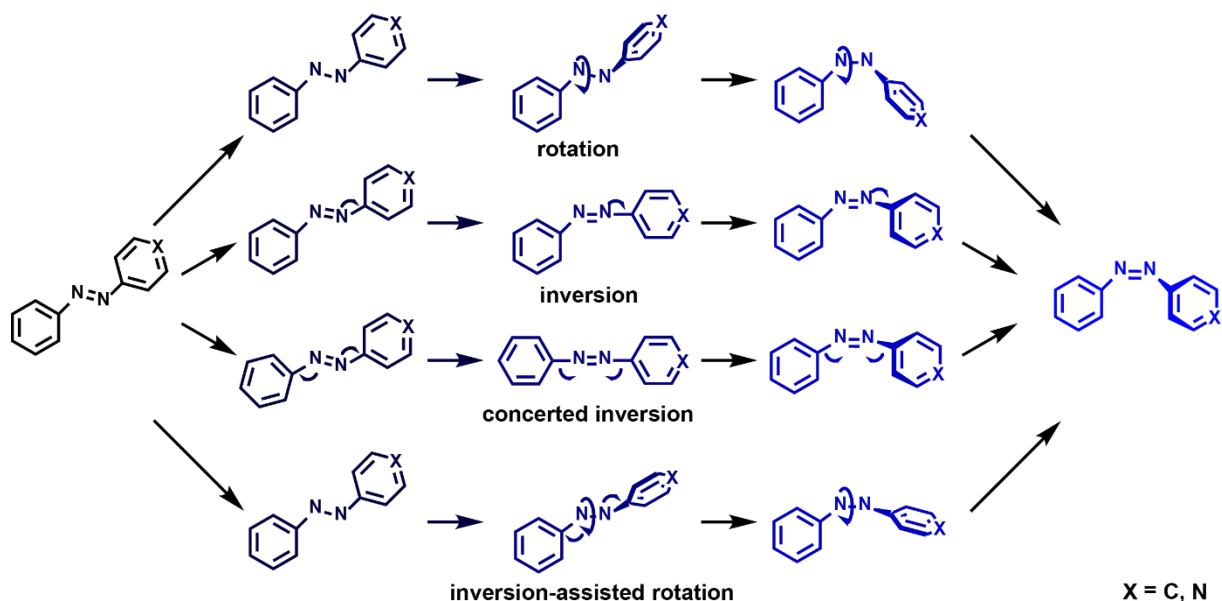
Table S2 summarizes the half-life values reported for studies of pH-dependent isomerization of azobenzene derivatives in water. Although still limited data is available for comprehensive studies in water for azobenzenes, the AAPs span a comparably large tunable area of ca. five orders of magnitude, while azobenzenes can be typically tuned within 2-3 decades. Additionally, the timescales for the AAP shifts towards longer timescales.

Table S2: Reported pH-tunable half-lives at 25 °C. While the half-life of AAP-PEG can be tuned over more than five orders of magnitude common azobenzene derivatives do not exceed four orders of magnitude and their half-lives are overall distinctly faster.

Structure	Reference	$\tau_{1/2}$ (min) (s)	$\tau_{1/2}$ (max) (s)
	This work	10^1	10^6
	[2]	10^2	10^3
	[2]	10^1	10^4
	[3]	10^{-6}	10^{-5}

	[4]	10^{-6}	10^{-2}
	[4]	10^{-5}	10^{-2}
	[4]	10^{-5}	10^{-3}
	[4]	10^{-5}	10^{-2}
	[5]	10^{-1}	10^1
	[6]	10^{-1}	10^1
	[6]	10^{-5}	10^{-2}
	[6]	10^{-5}	10^{-2}

Isomerization pathways of azobenzene and AAP



Scheme S2: Proposed photoisomerization mechanisms of azobenzene.^[7]

Computational thermochemistry

One obtains the internal energy $U(T)$ in dependence on temperature T from the electronic energy E via^[8]

$$U = E + E_{\text{ZPE}} + C_{V,\text{vib}}(T) \quad (5)$$

where both the zero-point energy E_{ZPE} as well as $C_{V,\text{vib}}(T)$ are determined from vibrational properties. Disregarding the contributions from pressure, one may approximate the Gibbs free energy as

$$G = U - T \cdot S \quad (6)$$

with the temperature $T = 298.15$ K (25°C) and the entropy S determined from vibrations. Note, that the electronic energy already contains approximate free energy contributions from the implicit solvent.^[9]

Evaluation of barriers: Unprotonated AAP

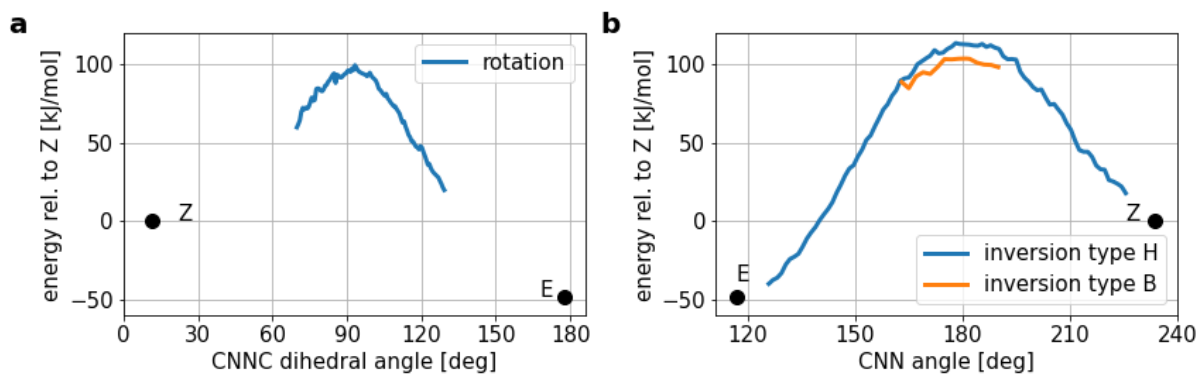


Figure S7: a) Electronic energy barrier for rotation in dependence of the CNNC dihedral angle. b) Barrier for inversion in dependence of the CNN angle (phenyl C for type B and heteroaryl for type H). The energies are given relative to the Z conformer.

We obtained the unprotonated rotation barrier by rotating the phenyl group around the central NN bond. We kept the CNNC dihedral angle fixed in each step while all other degrees of freedom were allowed to relax without symmetry constraints. The inversion barriers were probed by a stepwise increase of the CNN angle and relaxing all other degrees of freedom while keeping this angle fixed. Figure S7 shows the energies of the resulting paths in dependence of the CNNC dihedral angle and the CNN angle, respectively. The structure of maximal energy along the respective paths defines the corresponding transition state.

Table S3: Transition state structures and energies of the unprotonated AAPs. The structures marked with an asterisk are relaxed structures under a given constraint.


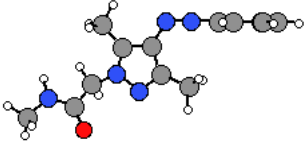
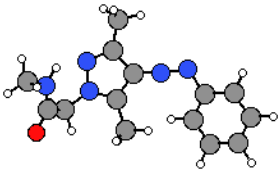
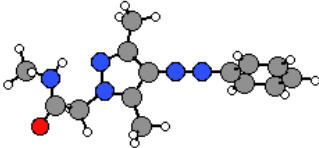
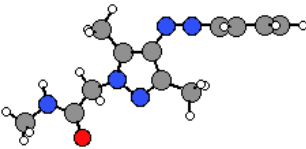
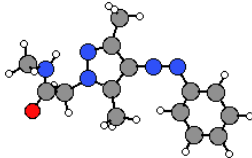
Structure	TS state	ΔE (kJ·mol ⁻¹)	ΔG (kJ·mol ⁻¹)
	rotation	102	98
	inversion type B	106	110
	inversion type H	115	106
	concerted inversion*	243	-
	inversion type B*	108	-
	inversion type H*	115	-

Table S3 lists the energies of the transition states for rotation. We cross checked the structures by comparing to proposed transition states from concerted inversion and the two inversion structures.^[10] The latter three structures were obtained by restricting the CNNC to be aligned (concerted inversion), the phenyl CNN to be aligned (inversion type B) and the heteroaryl CNN to be aligned (inversion type H). The latter structure

corresponds closely to the inversion structure we found. The overall energetically lowest barrier is that of rotation.

Table S4: The effect of the exchange-correlation functional on the barriers. Only electronic energies without zero-point corrections are reported (eq. 5)

TS state	PBE (kJ·mol ⁻¹)	TPSS ^a (kJ·mol ⁻¹)	M06-L ^a (kJ·mol ⁻¹)	PBE0 ^a (kJ·mol ⁻¹)	B3LYP ^a (kJ·mol ⁻¹)
rotation	102	111	118	440	369
inversion type B	106	111	119	163	151
inversion type H	115	119	129	147	139

^aDetermined from PBE densities and Kohn-Sham wave functions at PBE geometries

Table S4 shows the effect of the exchange-correlation functional on the barriers. While the semi-local generalized gradient approximation (GGA) PBE as well as the meta-GGAs TPSS and M06-L favor rotation, this barrier is clearly disfavored by hybrid functionals PBE0 and B3LYP.

Evaluation of barriers: Protonated AAP

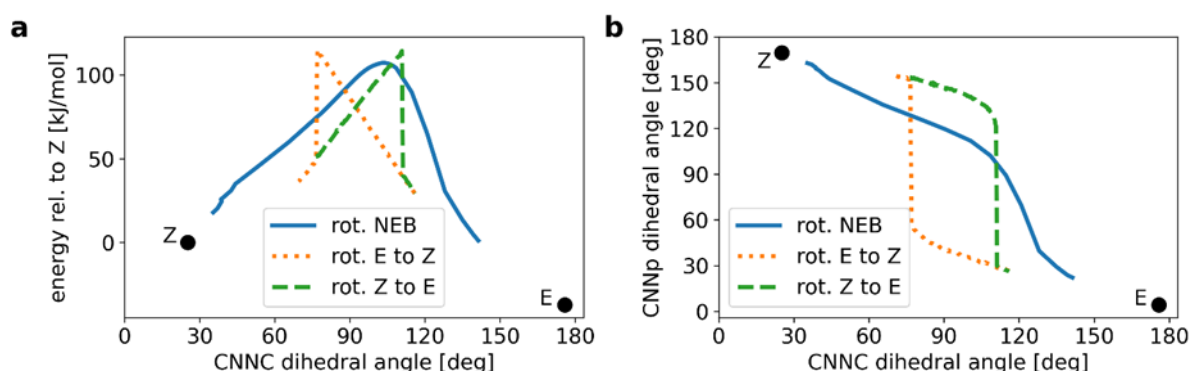


Figure S8: a) Electronic energy relative to the Z configuration for rotation. b) Hysteresis in the CNNp dihedral angle (p denoting the proton) during rotation.

We have applied the same strategy for the exploration of rotation and inversion barriers as in the unprotonated case. While this resulted in a path of continuous energy for inversion, we observed a discontinuity in case of rotation as displayed in Figure S8a. The energy increases when rotating from E to Z and sharply decreases around a dihedral angle of 70 deg. Rotating in the reversed direction shows the same sharp decrease in energy at a different dihedral angle. The discontinuity in energy is due the presence of the proton that flips from one to the other direction as displayed by the hysteresis in the heteroaryl CNNp (p denoting the proton) dihedral angle in Figure S8b. We doubted that the barrier to be overcome by temperature is not simply the maximal energy observed in these simulations and applied a search of the transition state through the nudged elastic band (NEB) method. The resulting barrier is displayed in Figure S8a also and is indeed 8 kJ/mol lower than the maxima obtained before. The NEB transition path shows a smooth transition in the CNNp dihedral angle (Figure S8b). Interestingly, the path is energetically higher than the path for rotation in a wide range of CNNC dihedral angles, but eventually allows for a lower transition state for rotation.

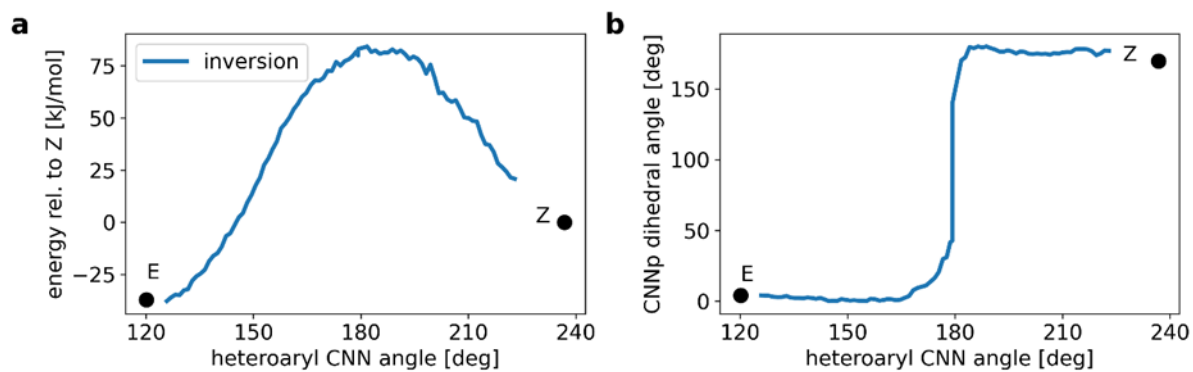


Figure S9: a) Electronic energy barrier for inversion in dependence of the CNN dihedral angle and b) the change in the CNNp dihedral angle.

The inversion path depicted in Figure S9a does not have the problem of a discontinuity in the energy. The maximum coincides with the rotation of the proton around the heteroaryl CNN angle of 180 deg (CNN inline configuration) as shown in Figure S9b.

Table S5: Transition state structures and energies in the protonated AAPs. The structures marked with an asterisk are relaxed structures under a given constraint.

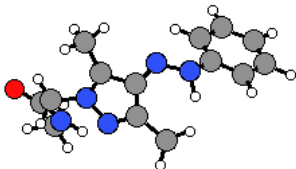
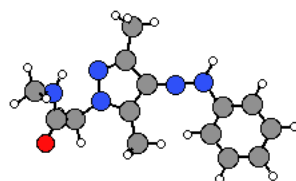
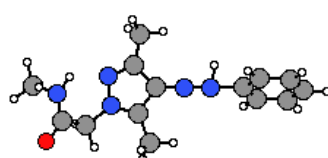
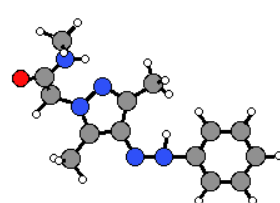
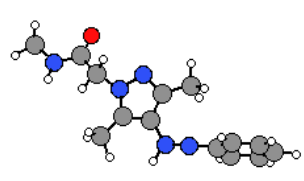
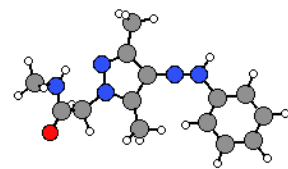
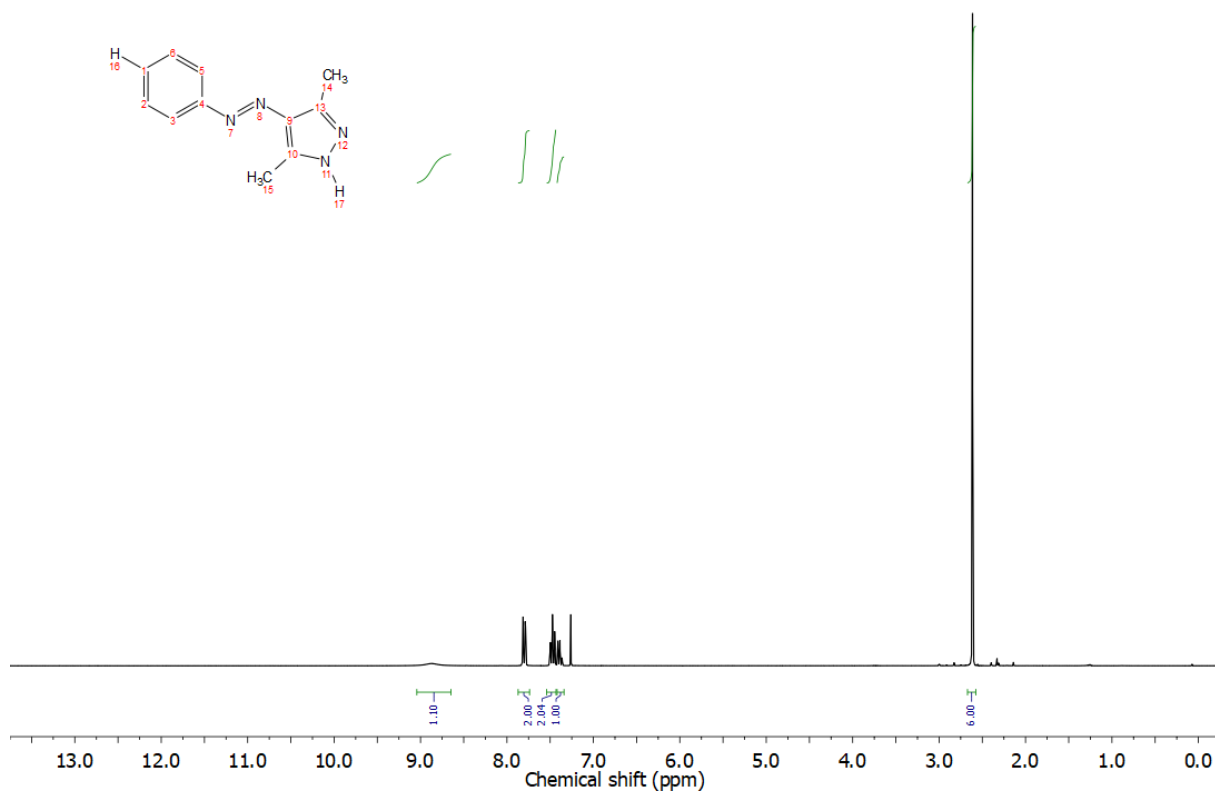
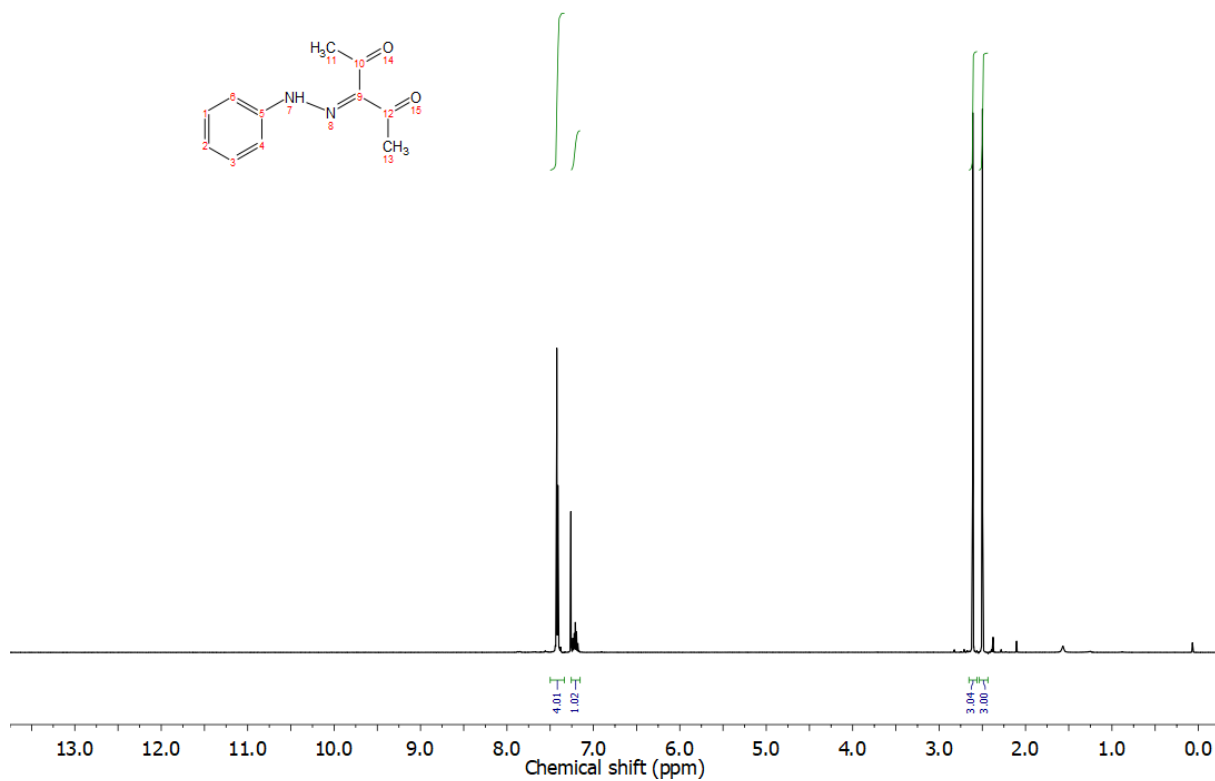
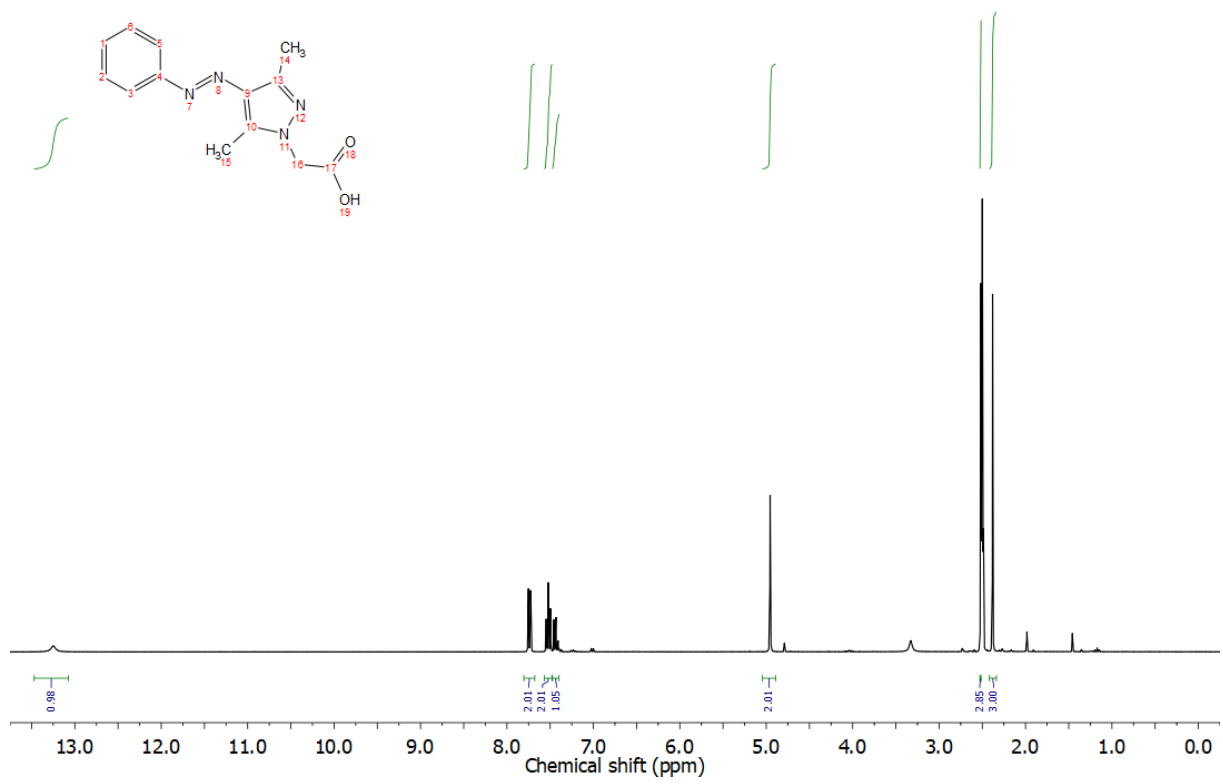
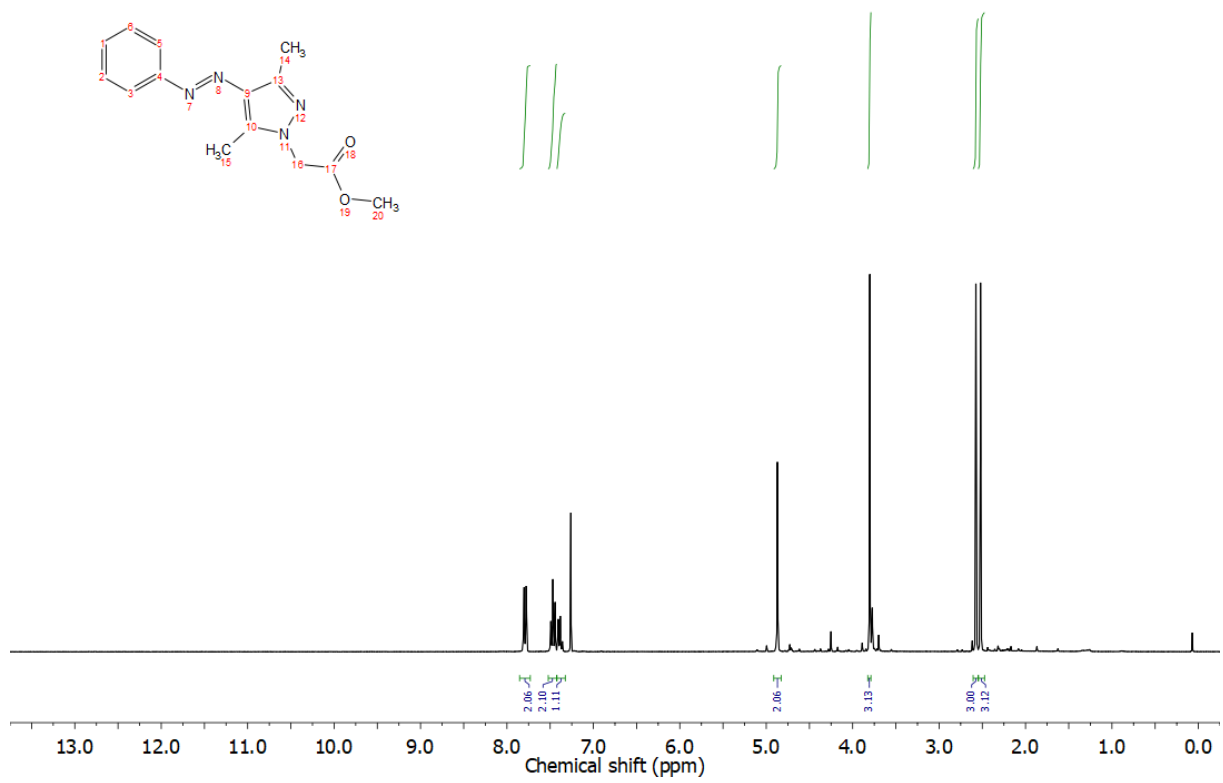
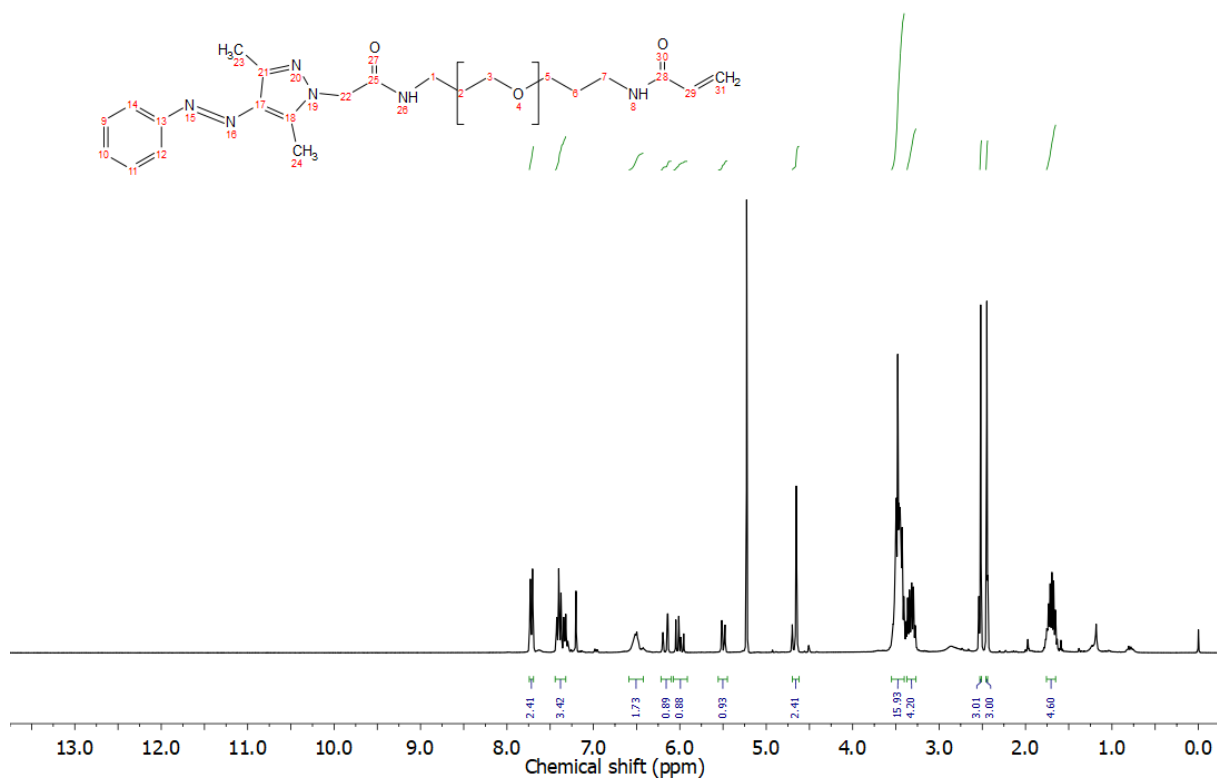
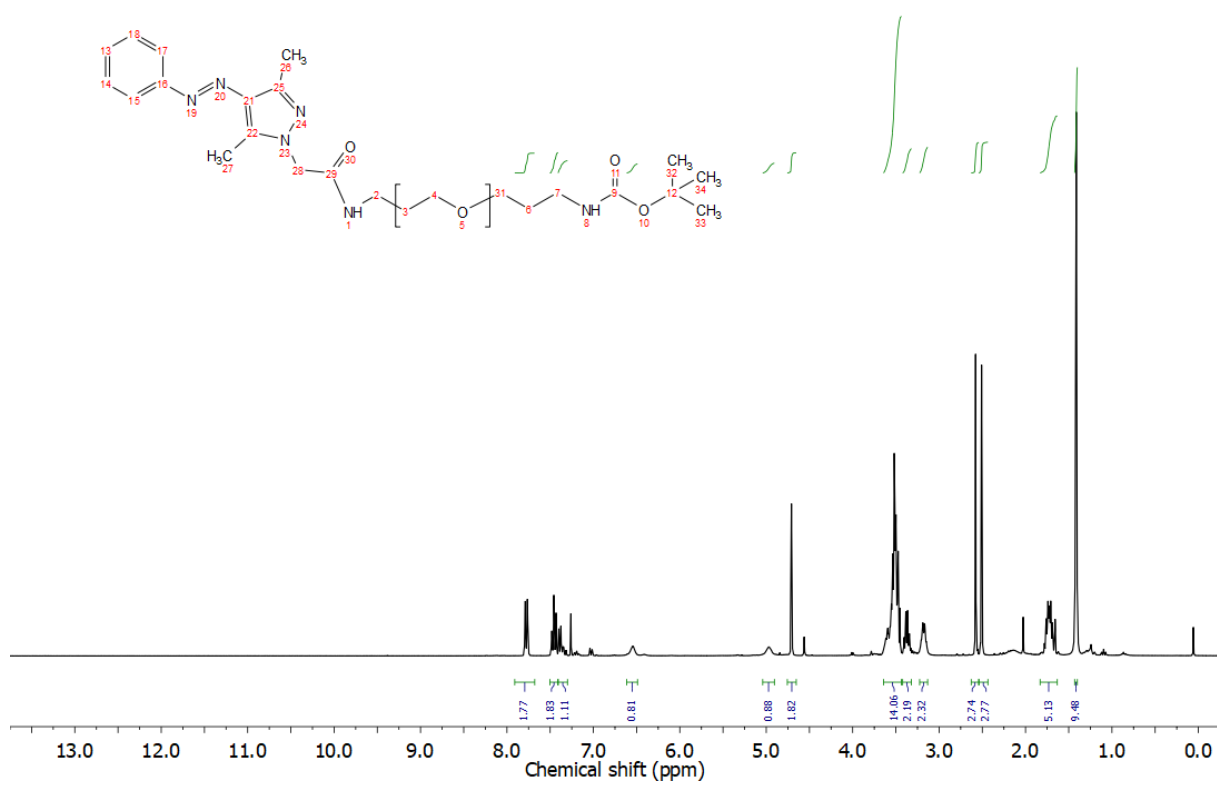
Structure	TS state	ΔE (kJ·mol ⁻¹)	ΔG (kJ·mol ⁻¹)
	rotation	93	84
	inversion type H	81	77
	concerted inversion*	372	-
	inversion type Ba*	240	-
	inversion type Bb*	153	-
	inversion type H*	90	-

Table S5 lists transitions states for protonated AAPs. The lowest transition state is found for inversion type H and possible inversion type B variants as well as concerted inversion can be ruled out as corresponding constrained optimization leads to structures of much higher energy.

Appendix







References

- [1] B. Wang, A. Walther, *ACS Nano* **2015**, *9*, 10637-10646.
- [2] R. Lovrien, J. C. Waddington, *J. Am. Chem. Soc.* **1964**, *86*, 2315-2322.
- [3] A. M. Sanchez, M. Barra, R. H. de Rossi, *J. Org. Chem.* **1999**, *64*, 1604-1609.
- [4] N. J. Dunn, W. H. Humphries IV, A. R. Offenbacher, T. L. King, J. A. Gray, *J. Phys. Chem. A* **2009**, *113*, 13144-13151.
- [5] S. Samanta, A. Babalhavaeji, M. X. Dong, G. A. Woolley, *Angew. Chem. Int. Ed.* **2013**, *52*, 14127-14130.
- [6] M. Dong, A. Babalhavaeji, M. Hansen, L. Kalman, G. Woolley, *Chem. Commun.* **2015**, *51*, 12981-12984.
- [7] H. D. Bandara, S. C. Burdette, *Chem. Soc. Rev.* **2012**, *41*, 1809-1825.
- [8] aC. J. Cramer, *Essentials of Computational Chemistry: Theories and Models*, John Wiley & Sons, **2013**;
bA. H. Larsen, J. J. Mortensen, J. Blomqvist, I. E. Castelli, R. Christensen, M. Dułak, J. Friis, M. N. Groves, B. Hammer, C. Hargus, *J. Phys. Cond. Mat.* **2017**, *29*, 273002.
- [9] A. Held, M. Walter, *J. Chem. Phys.* **2014**, *141*, 174108.
- [10] aJ. Calbo, C. E. Weston, A. J. P. White, H. S. Rzepa, J. Contreras-García, M. J. Fuchter, *J. Am. Chem. Soc.* **2017**, *139*, 1261-1274; bT.-T. Yin, Z.-X. Zhao, H.-X. Zhang, *New J. Chem.* **2017**, *41*, 1659-1669; cJ. Calbo, A. R. Thawani, R. S. Gibson, A. J. White, M. J. Fuchter, *Beilstein J. Org. Chem.* **2019**, *15*, 2753-2764.